*minerals*

MDPI

*Article*

# Physics-Informed Blind Hyperspectral Unmixing of Altered Minerals via Backscattering Parameter Learning

**Rui Xu [1,2], Houzhen Wei [1], Zhiguang Yang [3], Xiaolong Ma [1], Wentao Wang [1] and Yiteng Wang [1,*]**

[1] State Key Laboratory of Geomechanics and Geotechnical Engineering Safety, Institute of Rock and Soil Mechanics, Chinese Academy of Sciences, Wuhan 430071, China
[2] School of Engineering Sciences, University of Chinese Academy of Sciences, Beijing 100049, China
[3] School of Mathematics and Computer Science, Wuhan Polytechnic University, Wuhan 430048, China
* Correspondence: ytwang@whrsm.ac.cn

**Abstract**

The blind hyperspectral unmixing of altered minerals holds significant indicative importance for the exploration of sandstone-type uranium deposits. Nevertheless, the distinctive backscattering and multiphase characteristics are typically underestimated by existing methods, resulting in limited accuracy in the unmixing performance of complex mixtures. This study presents a physics-informed Swin Transformer Network (PIST–Net) for the blind hyperspectral unmixing of hematite, goethite, biotite, and chlorite. The proposed model includes a lightweight Swin Transformer encoder for the long-range modeling of spatial and spectral features. Furthermore, a dual-branch decoder with adaptive physical parameters was introduced in the spectral reconstruction section. In this decoder, the backscattering prediction head independently estimates the backscattering factor for each endmember, accounting for the true behavior of the mineral materials. As a key parameter of the Hapke model, the learnable strategy can reduce the spectral error in the single-scattering albedo (SSA) space to improve the accuracy of abundance estimation. The results show that PIST–Net consistently outperformed all six competing models on the altered mineral (AM) dataset and the NASA Reflectance Experiment Laboratory (RELAB) dataset. For mixtures composed of 2–4 endmembers, the mean RMSE of estimated abundances ranges from 0.0312 to 0.1037.

**Keywords:** altered mineral; short-wave infrared; blind hyperspectral unmixing; backscattering learning; Hapke model

Check for updates

Academic Editors: Lei Liu, Jingjing Dai and Yaqian Long

Received: 12 July 2026
Revised: 28 August 2026
Accepted: 31 August 2026
Published: 4 September 2026

**Copyright:** © 2026 by the authors. Licensee MDPI, Basel, Switzerland. This article is an open access article distributed under the terms and conditions of the Creative Commons Attribution (CC BY) license.

## 1. Introduction

In response to the rapidly growing demand for natural uranium, sandstone-type uranium deposits have emerged as a primary target for uranium mining [1–4]. The host rock of uranium deposits can be rapidly identified using the hyperspectral imaging (HSI), owing to the indication of uranium mineralization provided by specific altered minerals [5,6]. However, it is still a significant challenge to precisely quantify the composition of mixed altered minerals by utilizing the HSI method. One primary reason lies in the complexity of the mineral composition, characterized by uncertainties in type/proportion and spatial variability. Moreover, the intimate association between minerals could lead to multiple light scatterings, resulting in the nonlinear mixing characteristics in the spectrum [7–12]. Consequently, a blind and nonlinear hyperspectral unmixing method is essential for extracting the type and content of altered minerals.

In sandstone-type uranium deposits, uranium minerals typically coexist with specific altered minerals, which serve as clear indicators for the exploration. Evidence indicates that the uranium minerals are in close symbiotic association with ilmenite, pyrite, and clay minerals in the Pengyang uranium deposit of the Ordos Basin [13]. During uranium mineralization, hematite and goethite could be formed due to the reduction in dissolved uranyl ions by ferrous ions ($Fe^{2+}$) derived from ilmenite [14–16]. In particular, in uranium-bearing gray sandstones, pyrite is one of the primary metallic sulfides and is intimately associated with uranium mineralization [17–20]. Abundant ilmenite and pyrite were also identified in mineralized gray sandstones, where their reducing nature is essential for the precipitation and formation of uranium minerals. Beyond ilmenite and pyrite, alteration minerals symbiotic with uranium minerals further include biotite and chlorite. The strong reducing capability of pyrite provides a vital micro-reduction environment for uranium mineralization, while altered ilmenite and biotite additionally contribute to uranium adsorption and storage [21]. Yue et al. [22] suggest that the mineral composition of sandstones in uranium deposits reflects oxidation–reduction conditions associated with uranium mineralization and thereby manifests distinct color characteristics. Sandstones exhibiting red, yellow, and green colors due to oxidizing alteration generally comprise hematite, goethite, and chlorite as one of their primary constituents. Furthermore, these colorful sandstones typically act as the key pathways for uranium activation and migration within roll-type uranium deposits controlled by the oxidation front [23–27]. Consequently, it is crucial to estimate the composition and content of these altered minerals related to the uranium mineralization for locating the uranium ore bodies.

Owing to the intimate association between altered minerals, substantial pixels resulting from nonlinear mixing of endmember spectra are present in the HSI data. Therefore, the sub-pixel alteration information can only be extracted from mixed pixels through spectral unmixing. Based on the pure-pixel assumption, Ishidoshiro et al. [28] applied the Improved Causal Random Pixel Purity Index (ICRPPI) method to extract endmember spectra of clay minerals, while the abundance of each mineral was estimated by the Linear Spectral Unmixing (LSU) [29]. In the research by Soydan et al. [30], the Simplex Identification via Split Augmented Lagrangian (SISAL) and the Minimum Volume Simplex Algorithm (MVSA) identified the endmember using the iron-induced absorption features of secondary iron minerals between 700 and 900 nm. The correlation of abundance obtained by the SISAL reached 0.76 with spectral angle errors consistently below 0.1, and it outperformed the MVSA method at all spatial resolutions employed. Subsequently, the abundance estimation was performed using the Fully Constrained Least Squares (FCLS) algorithm, which strictly satisfies the Abundance Nonnegativity Constraint (ANC) and the Abundance Sum-to-One Constraint (ASC). Compared to the ICRPPI, the SISAL and MVSA methods overcome the restrictions of the pure-pixel assumption and demonstrate improved robustness to noise. The Mixture Tuned Matched Filtering (MTMF) [31–36] method is known to be effective in identifying intimate oxidation and hydrothermal altered minerals. Throughout the spectral unmixing process, the MTMF calculates the MF scores of pixel spectra relative to specific endmember spectra and further estimates the subpixel abundance of these endmembers. It makes the MTMF-based spectral unmixing dependent on the specified endmember spectra. For instance, Muavhi [37] integrated PPI-based endmember extraction into the MTMF algorithm, achieving the extraction of two alteration mineral assemblages (chlorite-epidote and sericite-muscovite) along with their abundance data from the Advanced Spaceborne Thermal Emission and Reflection Radiometer (ASTER) dataset. Moghadam et al. [38] comparatively evaluated the performance of five linear unmixing methods, which are combinations of the FCLS with Pixel Purity Index (PPI), N-FINDR, Vertex Component Analysis (VCA), Sequential Maximum Angle Convex Cone (SMACC),

and Simplex Growing Algorithm (SGA). From the perspective of the endmember spectrum, the VCA and the N-FINDR exhibit optimal performance on their own datasets. In recent studies, machine learning (ML) approaches such as random forests (RF) [39], support vector machines (SVM) [40], pattern recognition networks [41], and stacking autoencoders (SAE) [42] have been widely utilized for spectral unmixing of altered minerals. Compared to the Linear Mixing Model (LMM), machine learning methods are more effective at extracting nonlinear features from the spectra of mixtures, such as the multiple scattering between granular materials. However, numerous ML-based spectral unmixing methods are supervised (i.e., non-blind or semi-blind), which means they are driven by large and high-quality annotated data. Such data is typically scarce in the field of hyperspectral remote sensing. Furthermore, ML methods are commonly criticized for their insufficient physical interpretability.

To address these limitations, this study built a hyperspectral dataset of uranium-related altered mineral (AM) dataset, including hematite, goethite, biotite, and chlorite. Furthermore, a physics-informed Swin Transformer Network (PIST–Net) was developed for the blind hyperspectral unmixing. The PIST–Net integrated a dual-branch decoder with adaptive physical parameters to account for mineral-specific scattering characteristics. Within the decoder, each backscattering factor was independently predicted by a backscattering prediction head, which also provided key material parameters for the Hapke model. This adaptive approach could increase the calculation accuracy of single-scattering albedo (SSA), thereby improving the unmixing performance and generalization capability of the network. On the AM dataset and the NASA Reflectance Experiment Laboratory (RELAB) dataset, PIST–Net was evaluated and compared with six advanced blind unmixing models.

## 2. Materials and Methods

### *2.1. The Proposed Method*

As shown in Figure 1, the input hyperspectral data $\boldsymbol{Y}$ is a preprocessed 3D array with dimensions of $H$ (height) $\times$ $W$ (width) $\times$ $N$ (number of bands). To begin with, the hyperspectral data is partitioned into multiple non-overlapping patches along the $H$ and $W$ dimensions. These patches are then input into a lightweight two-stage Swin Transformer encoder for patch embedding and feature extraction. The feature $\boldsymbol{F}$ with dimensions $H/4 \times W/4 \times 2C$ is obtained through the feature extraction procedure, where $C$ is the embedding dimension. In the output process, this feature is utilized to estimate the abundance map $\boldsymbol{A}$ and the backscattering factor $\boldsymbol{B}$ through the abundance projection head and the backscattering projection head, respectively. In particular, the last dimension $R$ of $\boldsymbol{A}$ and $\boldsymbol{B}$ is identical to the number of endmembers. Afterwards, the abundance map $\boldsymbol{A}$ is used to generate the reconstructed hyperspectral data $\boldsymbol{Y}_{\mathbf{est}}$ through a convolutional layer, while the endmember spectrum $\boldsymbol{E}$ represented by reflectance is derived from the weights. Meanwhile, the abundance map $\boldsymbol{A}$ is also utilized to compute the physical hyperspectral data f ($f^{-1}(\boldsymbol{E})\boldsymbol{A}$), where the $f^{-1}(\boldsymbol{E})$ represents the projection of $\boldsymbol{E}$ onto the SSA space. This projection employed the Hapke bidirectional reflection model with incident angle, exit angle, and phase angle all set to 0, as shown in Equation (1):

$$r = f(w) = (w/8\pi)\left[(1+b)p + 9/\left(1+2\sqrt{1-w}\right)^2 - 1\right], \quad (1)$$

where $r$ is the reflectance; $w$ is the SSA; $b$ is the backscattering factor of the endmember; and $p$ is the phase factor. Specifically, $b$ is an empirical factor representing the amplitude of the opposition effect. It is derived from the backscattering function $B(g)$ in the Hapke bidirectional reflectance (BDRF) model [43] with its values ranging from 0 to 1. Likewise, $p$

is derived from the phase function $p(g)$ of the particles, with values ranging from −1 to 1. Under the assumption of isotropic scattering, $p$ uniformly takes the value of 1.

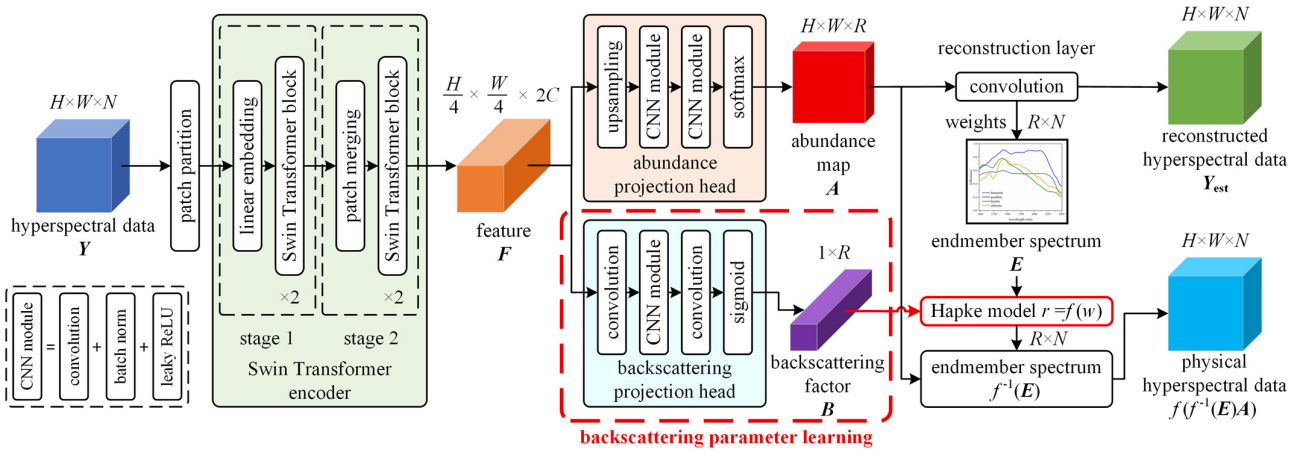


**Figure 1.** Architecture of the PIST–Net.

The loss function adopted in this study is composed of the reconstruction loss and the physical loss, as shown in Equation (2):

$$\mathcal{L}(\mathbf{Y}, \boldsymbol{Y}_{\mathbf{est}}, \boldsymbol{E}, \boldsymbol{A}) = \|\boldsymbol{Y}_{\mathbf{est}} - \boldsymbol{Y}\|_F^2/2 + \alpha \cdot \left\| R\left(R^{-1}(\boldsymbol{E})\boldsymbol{A}\right) - \boldsymbol{Y} \right\|_F^2/2, \quad (2)$$

where $\mathcal{L}(\mathbf{Y}, \boldsymbol{Y}_{\mathbf{est}}, \boldsymbol{E}, \boldsymbol{A})$ is the loss function; $\|\cdot\|_F$ refers to the Frobenius norm; and $\alpha$ is the coefficient of the physical loss. Within the loss function, the first term represents the reconstruction loss, the second term represents the physical loss, and the ratio between them can be controlled by the coefficient $\alpha$. The primary hyperparameters used in the PIST–Net were determined through a basic grid search, as shown in Table 1.

**Table 1.** The primary hyperparameters used in the PIST–Net.

| Locations | Hyperparameters | Values | | |
|---|---|---|---|---|
| | | **Binary** | **Ternary** | **Quaternary** |
| Swin Transformer encoder | Image size ($H \times W$) | 30 × 30 | 30 × 50 | 20 × 25 |
| | Patch size | 2 × 2 | 2 × 2 | 5 × 5 |
| | Input channel | | 256 | |
| | Embedding dimension $C$ | | 128 | |
| | Depths | | 2, 2 | |
| | Number of heads | | 4, 8 | |
| | Window size | | 2 × 2 | |
| Abundance projection head<br>Backscattering projection head<br>Reconstruction layer | Input/output channel | | 256, 64, 32, 4<br>256, 32, 16, 4<br>4, 256 | |
| Loss function | Coefficient $\alpha$ | 0.001 | 0.001 | 0.0001 |
| Training | Learning rate | | 0.0005 | |
| | Iterations | | 10,000 | |

### *2.2. Sample Preparation, Data Acquisition and Preprocessing*

Four altered minerals were selected as endmembers in this study, including hematite, goethite, biotite, and chlorite. All materials had purity exceeding 99% and were passed through a 200 μm sieve after oven-drying to mitigate the particle size effects on spectroscopy. Four pure mineral samples were first prepared to quantitatively evaluate the endmember

spectrum. For mixed mineral samples, they were uniformly blended from pure minerals according to the predefined mass fractions. The step size of the mass fractions was fixed at 1/7. As a result, 116 mixed mineral samples were obtained, which consisted of 36 binary mineral samples, 60 ternary mineral samples, and 20 quaternary mineral samples (Figure 2). All pure and mixed mineral samples have a uniform diameter of 32 mm and a mass of 2.5 $\pm$ 0.005 g. Prior to data acquisition, all samples were vibrated to flatten their surfaces.

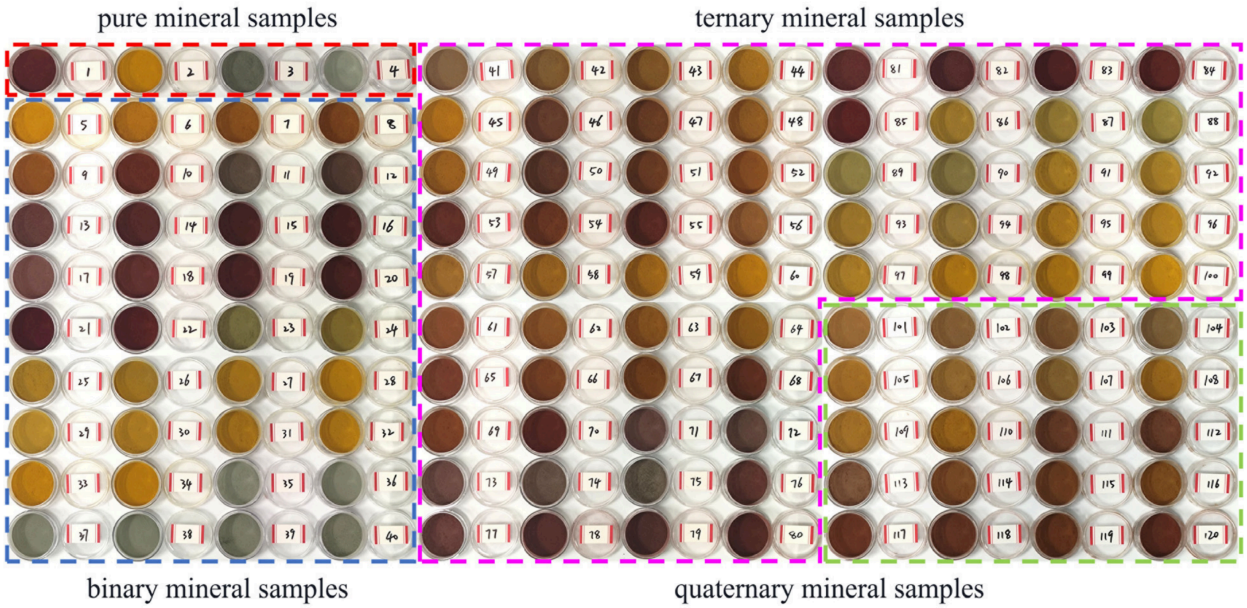


**Figure 2.** Pure and mixed mineral samples.

The hyperspectral data of these mineral samples were acquired using a short-wave infrared (SWIR) hyperspectral camera (Dualix Spectral Imaging, Wuxi, China) integrated with a servo-driven scanning system. Specifically, the effective spectral range, spectral resolution (FWHM), and number of bands are 978–2508 nm, 10 nm, and 256, respectively. Before each spectral scan, white reference and systematic noise data were collected for the radiometric calibration of hyperspectral imaging data. Specifically, the white reference data was quired on a standard white board coated with polytetrafluoroethylene (PTFE), which has a typical diffuse reflectance of 99%. Reflectance in radiometric calibration was calculated by Equation (3):

$$r = \rho(I - I_d)/(I_w - I_d), \tag{3}$$

where $r$ is the reflectance; $\rho$ is the reflectance ratio; and $I$, $I_w$, and $I_d$ are the corresponding pixel values in the hyperspectral imaging data, white reference data, and systematic noise data, respectively. Each pixel spectrum of the hyperspectral data was individually normalized to the range of 0 to 1. Thereafter, a data block with 5 $\times$ 5 pixels were extracted from the central region of each data to minimize environmental influences and improve unmixing efficiency. These data blocks were further classified and assembled according to the mixing pattern of minerals, resulting in the hyperspectral data for the blind unmixing. Additionally, the ground truth of endmember spectra and abundance maps were employed for result evaluation (Table 2). Each ground truth of an endmember spectrum was averaged from 1250 spectra of pure minerals (Figure 3), while the ground truth of abundance maps was synthesized based on the mass contents. In this work, the hyperspectral data, along with the ground truth of endmember spectra and abundance maps, are collectively referred to the AM dataset, including a binary, a ternary, and a quaternary hyperspectral data.

**Table 2.** Characteristics of the AM dataset.

| Type of the Hyperspectral Data | Arrangement of Data Blocks | Shape of the Hyperspectral Data ($N \times H \times W$) | Shape of the Abundance Map ($R \times H \times W$) |
|---|---|---|---|
| Binary | 6 × 6 | 256 × 30 × 30 | 4 × 30 × 30 |
| Ternary | 6 × 10 | 256 × 30 × 50 | 4 × 30 × 50 |
| Quaternary | 4 × 5 | 256 × 20 × 25 | 4 × 20 × 25 |

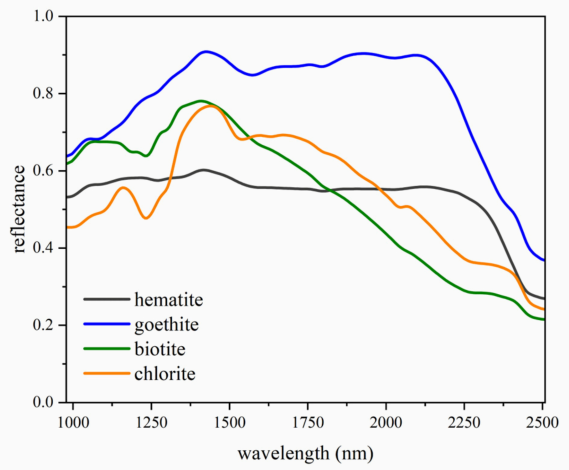


**Figure 3.** The ground truth of endmember spectra in the AM dataset.

The hyperspectral data in the AM dataset includes three types: binary, ternary, and quaternary type. It represents the number of endmembers in each spectrum. All four endmembers simultaneously exist within each type of the hyperspectral data and each of its individual data blocks. Figure 4 presents the expanded ground truth of abundance maps, where possible abundance values include multiples of 1/7 in the range of 0 to 1. For the binary and ternary abundance maps, two and three endmembers with positive abundance values exist in each data block, respectively. This indicates that the endmembers corresponding to the positive abundance are activated in the hyperspectral data, while those with zero abundance are absent. For the same reason, all values in the quaternary abundance maps exceed 0.

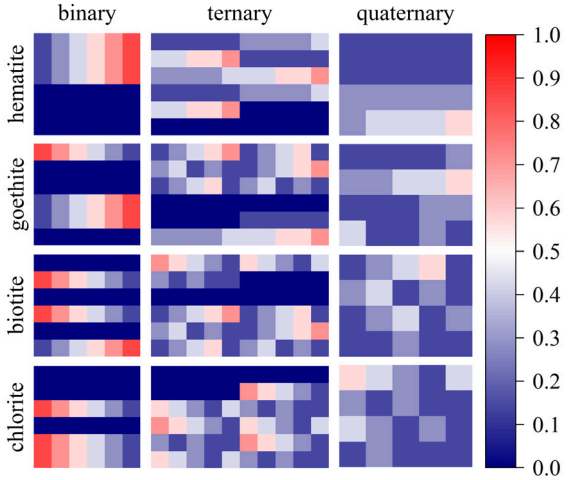


**Figure 4.** The ground truth of abundance maps in the AM dataset.

### *2.3. Noisy Dataset Synthesis*

To assess the noise robustness of the PIST–Net and the competing models, Gaussian noise was added to the binary hyperspectral data. The resulting noisy dataset comprised four noise levels with signal-to-noise ratios (SNR) of 20, 30, 40, and 50 dB. The SNR was calculated by Equation (4):

$$snr = 10 \log_{10}(P_s / P_n), \quad (4)$$

where $snr$ is the SNR of the binary hyperspectral data; $P_s$ is average power of the spectra; and $P_n$ is average power of the Gaussian noise. The calculation and addition of the Gaussian noise were performed independently for each band, with a mean of 0 and a standard deviation (SD) of $P_n^{1/2}$. Figure 5 presents the spectra of the top-left pixel before and after adding noise to the binary hyperspectral data. The raw pixel spectrum is assumed to be noise-free and referred to as the baseline. The noisy spectrum with $snr$ = 50 dB has a highly similar shape to the baseline, with a spectral angle distance (SAD) of only $2.80 \times 10^{-3}$ rad. This indicates that the SNR of the hyperspectral data in the AM dataset is significantly superior to 50 dB. As the SNR decreases, the noisy spectra exhibit serrated fluctuations and gradually intensify, with the SAD surging to $9.60 \times 10^{-2}$ rad in the 20 dB scenario. Considering the changes in reflectance resulting from the introduced noise, the hyperspectral data were subsequently clipped to the theoretical range of 0 to 1.

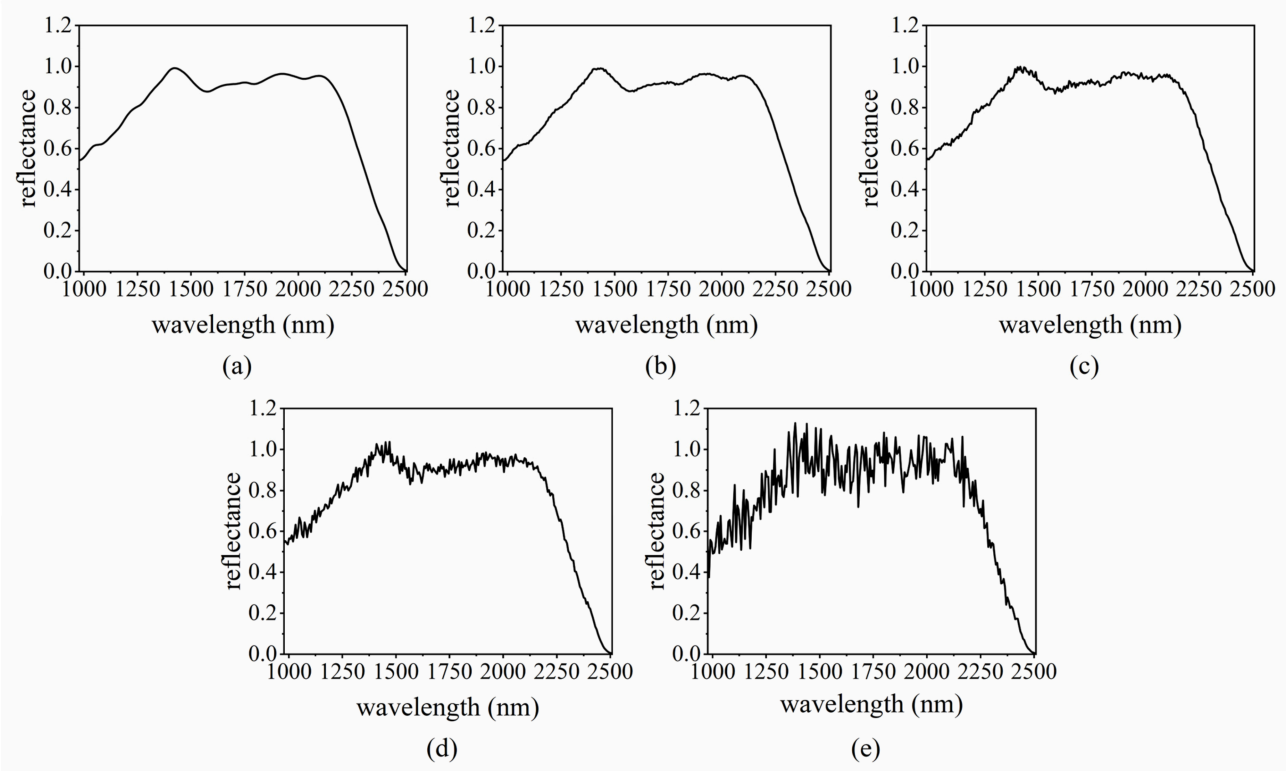


**Figure 5.** Noisy spectra at different SNR levels: (**a**) baseline; (**b**) $snr$ = 50 dB; (**c**) $snr$ = 40 dB; (**d**) $snr$ = 30 dB; and (**e**) $snr$ = 20 dB.

## 3. Results and Discussion

### *3.1. AM Dataset*

To evaluate the performance of the PIST–Net proposed in this study, six advanced blind unmixing models were utilized for the comparative analysis. UnDIP [44]: A deep learning method that combines simplex volume maximization (SiVM) [45] and deep image prior, dedicated to linear endmember extraction and abundance estimation, respectively. NMF–QMV [46]: A linear method that jointly optimizes elements and abundances by variational

minimum volume (MV) regularization. HapkeCNN [47]: A nonlinear blind unmixing model based on the Physics-Informed Neural Networks (PINN) framework, incorporating a convolutional autoencoder (CAE) for the feature extraction. UNMamba [48]: An improved linear model incorporating state-space models (SSMs) to capture global features with reduced computational complexity. Specifically, the downsampling ratios of the UNMamba model were adjusted to 16, 10, and 5 to accommodate the binary, ternary, and quaternary data, respectively. DeepTrans [49]: A hybrid network capturing multi-scale spatial–spectral features using both CAE and Transformer architectures. MiSiCNet [50]: A Minimum Simplex Convolutional Network integrating spectral, spatial, and geometric information. SAD and root mean square error (RMSE) are selected to evaluate the endmember spectra and the abundance maps, respectively. The value of SAD ranges from 0 to $\pi/2$, while the RMSE ranges from 0 to 1 due to the ANC and ASC inherent in the abundance maps.

#### 3.1.1. Binary Hyperspectral Data

Figures 6 and 7 show estimated endmember spectra and abundance maps based on the binary hyperspectral data, including their visual comparison with the ground truth. The results indicate that PIST–Net outperforms all six competing models in terms of blind unmixing performance on the binary AM dataset. For hematite, goethite, biotite, and chlorite, there are no significant differences between the estimated results and the ground truth. Tables 3 and 4 present SAD and RMSE for the preceding results, corresponding to the statistical errors in the spectra and abundance maps, respectively. PIST–Net achieved a mean SAD of 0.0212 and a mean RMSE of 0.0312, with well-balanced performance across four endmembers. Among these, the estimation error for hematite and chlorite ranked second among all models, slightly larger than the result of the second-best model termed UnDIP. Comparatively, the two errors of PIST–Net decreased remarkably by 34.4% and 49.6%, respectively. NMF–QMV ranked as the third-best model with a mean RMSE of 0.1145. Nevertheless, there are indistinct boundaries between certain adjacent regions, indicating that NMF–QMV exhibits insufficient ability to distinguish data with similar abundances (Figure 7). According to the abundance map, the unmixing results of HapkeCNN substantially deviate from the ground truth. This deviation may result from all backscattering factors of the endmembers being fixed to 0.

**Table 3.** SAD results for the binary hyperspectral data (the best performances are shown in bold).

| Endmember | PIST–Net | UnDIP | NMF–QMV | HapkeCNN | UNMamba | DeepTrans | MiSiCNet |
|---|---|---|---|---|---|---|---|
| Hematite | 0.0254 ± 0.0024 | **0.0151 ± 0.0000** | 0.0750 ± 0.0000 | 0.0476 ± 0.0001 | 0.0725 ± 0.0193 | 0.0576 ± 0.0064 | 0.0941 ± 0.0000 |
| Goethite | **0.0102 ± 0.0005** | 0.0574 ± 0.0000 | 0.0904 ± 0.0000 | 0.0321 ± 0.0000 | 0.1209 ± 0.0153 | 0.0647 ± 0.0012 | 0.1798 ± 0.0000 |
| Biotite | **0.0164 ± 0.0006** | 0.0258 ± 0.0000 | 0.1346 ± 0.0000 | 0.0256 ± 0.0000 | 0.0536 ± 0.0057 | 0.0971 ± 0.0044 | 0.1702 ± 0.0000 |
| Chlorite | 0.0328 ± 0.0011 | **0.0311 ± 0.0000** | 0.0846 ± 0.0000 | 0.1015 ± 0.0002 | 0.1387 ± 0.0052 | 0.0834 ± 0.0027 | 0.1316 ± 0.0000 |
| Mean | **0.0212 ± 0.0008** | 0.0323 ± 0.0000 | 0.0962 ± 0.0000 | 0.0517 ± 0.0001 | 0.0964 ± 0.0026 | 0.0757 ± 0.0015 | 0.1439 ± 0.0000 |

**Table 4.** RMSE results for the binary hyperspectral data (the best performances are shown in bold).

| Endmember | PIST–Net | UnDIP | NMF–QMV | HapkeCNN | UNMamba | DeepTrans | MiSiCNet |
|---|---|---|---|---|---|---|---|
| Hematite | **0.0330 ± 0.0020** | 0.0656 ± 0.0000 | 0.1147 ± 0.0000 | 0.2370 ± 0.0002 | 0.2135 ± 0.0124 | 0.3204 ± 0.0123 | 0.2742 ± 0.0000 |
| Goethite | **0.0233 ± 0.0011** | 0.0696 ± 0.0000 | 0.1146 ± 0.0000 | 0.1571 ± 0.0000 | 0.1894 ± 0.0151 | 0.2448 ± 0.0138 | 0.2824 ± 0.0000 |
| Biotite | **0.0321 ± 0.0025** | 0.0625 ± 0.0001 | 0.1143 ± 0.0000 | 0.1237 ± 0.0001 | 0.3209 ± 0.0316 | 0.2553 ± 0.0102 | 0.3835 ± 0.0000 |
| Chlorite | **0.0365 ± 0.0025** | 0.0496 ± 0.0000 | 0.1146 ± 0.0000 | 0.1903 ± 0.0002 | 0.2631 ± 0.0211 | 0.2437 ± 0.0173 | 0.3801 ± 0.0000 |
| Mean | **0.0312 ± 0.0018** | 0.0619 ± 0.0000 | 0.1145 ± 0.0000 | 0.1770 ± 0.0001 | 0.2467 ± 0.0096 | 0.2660 ± 0.0082 | 0.3300 ± 0.0000 |

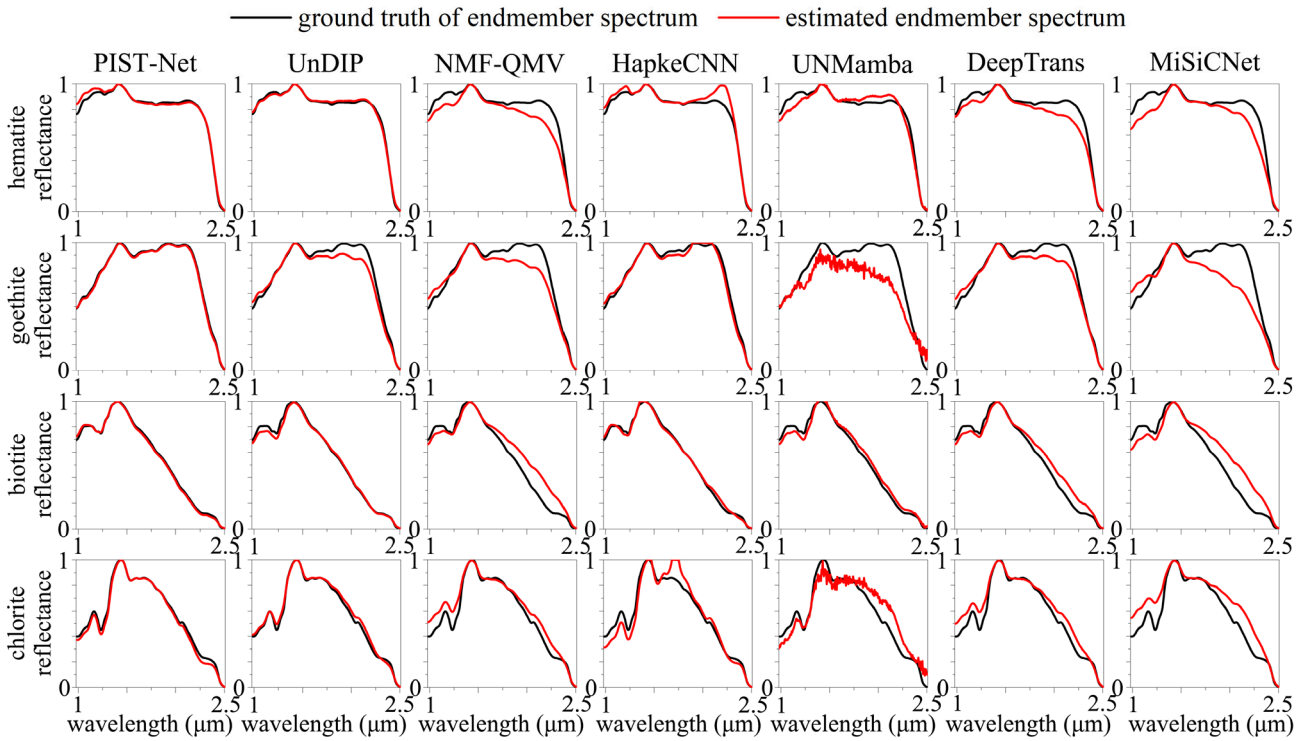


**Figure 6.** Visual comparison of estimated endmember spectra using the binary hyperspectral data.

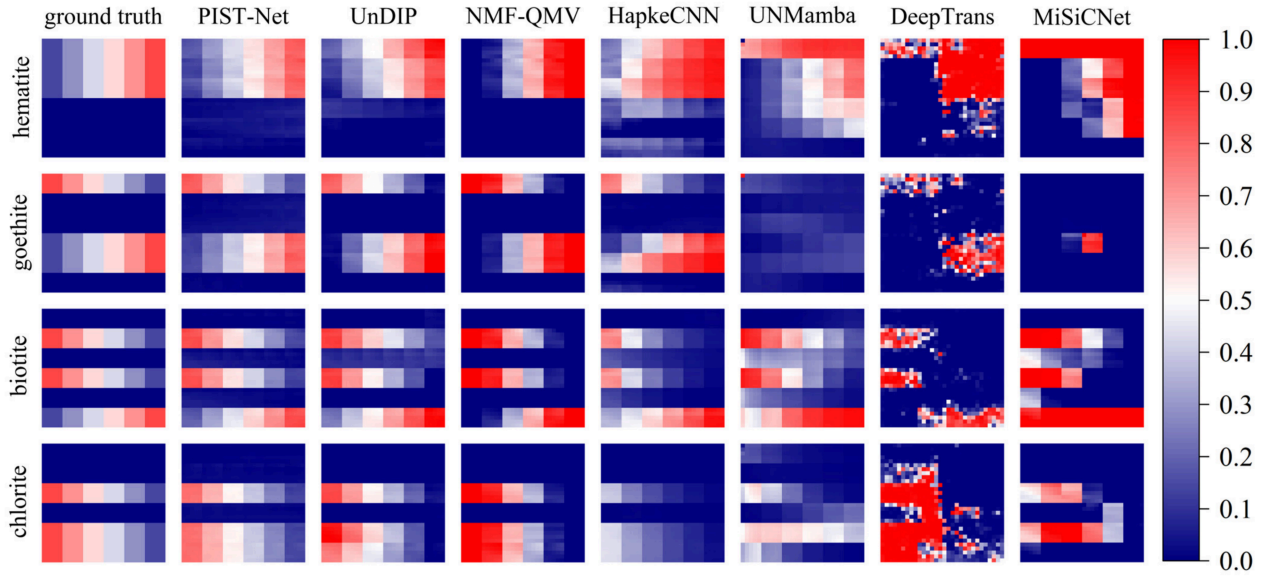


**Figure 7.** Visual comparison of estimated abundance maps using the binary hyperspectral data.

### 3.1.2. Ternary Hyperspectral Data

The visualization of the unmixing results for the ternary hyperspectral data is shown in Figures 8 and 9. For the ternary hyperspectral data, PIST–Net consistently demonstrates superior unmixing performance over all competing models, being the only model with a mean RMSE below 0.1. As the number of endmembers increased from 2 to 3, the two errors of PIST–Net increased by 0.0080 and 0.0044, respectively. In contrast, the second-best model was UnDIP, which experienced increments of 0.0289 and 0.0454, respectively. This indicates that PIST–Net achieves excellent unmixing accuracy and robustness to mixing complexity. Among all seven models, PIST–Net, UnDIP, and NMF–QMV outperformed the other four models in terms of abundance estimation (Tables 5 and 6).

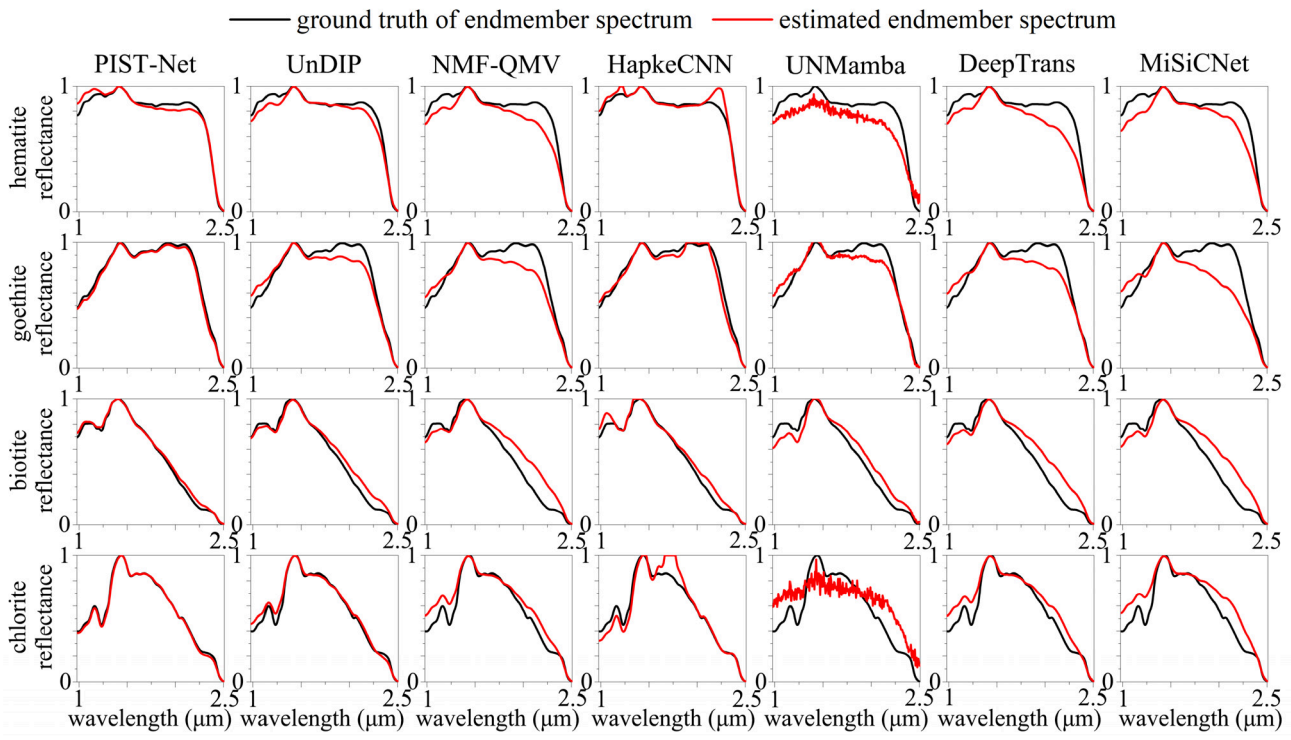


**Figure 8.** Visual comparison of estimated endmember spectra using the ternary hyperspectral data.

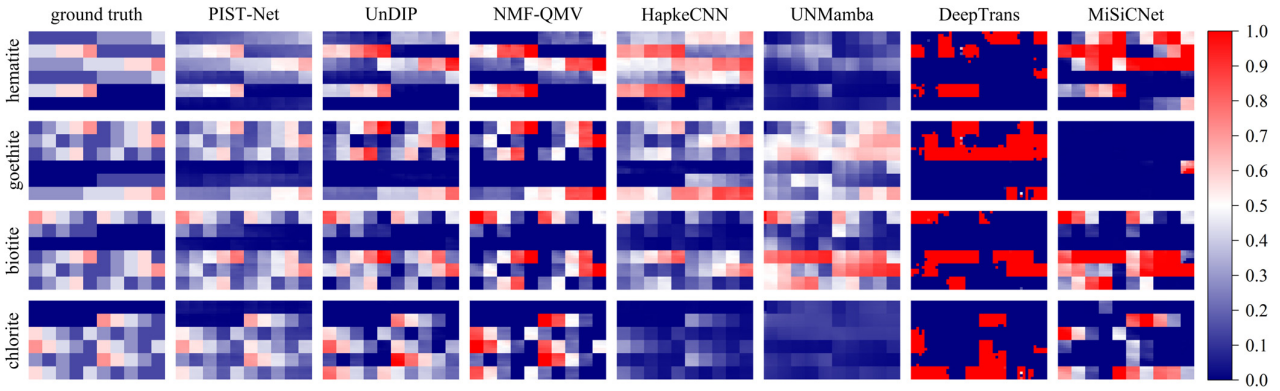


**Figure 9.** Visual comparison of estimated abundance maps using the ternary hyperspectral data.

**Table 5.** SAD results for the ternary hyperspectral data (the best performances are shown in bold).

| Endmember | PIST–Net | UnDIP | NMF–QMV | HapkeCNN | UNMamba | DeepTrans | MiSiCNet |
|---|---|---|---|---|---|---|---|
| Hematite | 0.0452 ± 0.0029 | **0.0439± 0.0000** | 0.0860 ± 0.0000 | 0.0512 ± 0.0001 | 0.0935 ± 0.0117 | 0.1051 ± 0.0060 | 0.0998 ± 0.0000 |
| Goethite | **0.0193 ± 0.0021** | 0.0767 ± 0.0000 | 0.1034 ± 0.0000 | 0.0483 ± 0.0000 | 0.0956 ± 0.0260 | 0.1019 ± 0.0016 | 0.1811 ± 0.0002 |
| Biotite | **0.0323 ± 0.0005** | 0.0762 ± 0.0000 | 0.1544 ± 0.0000 | 0.0611 ± 0.0001 | 0.1314 ± 0.0120 | 0.1538 ± 0.0032 | 0.1838 ± 0.0000 |
| Chlorite | **0.0199 ± 0.0014** | 0.0480 ± 0.0000 | 0.0970 ± 0.0000 | 0.1011 ± 0.0002 | 0.2284 ± 0.0160 | 0.1025 ± 0.0028 | 0.1343 ± 0.0000 |
| Mean | **0.0292 ± 0.0005** | 0.0612 ± 0.0000 | 0.1102 ± 0.0000 | 0.0654 ± 0.0001 | 0.1372 ± 0.0074 | 0.1158 ± 0.0016 | 0.1498 ± 0.0001 |

**Table 6.** RMSE results for the ternary hyperspectral data (the best performances are shown in bold).

| Endmember | PIST–Net | UnDIP | NMF–QMV | HapkeCNN | UNMamba | DeepTrans | MiSiCNet |
|---|---|---|---|---|---|---|---|
| Hematite | **0.0243 ± 0.0011** | 0.1079 ± 0.0000 | 0.1465 ± 0.0000 | 0.2186 ± 0.0003 | 0.2810 ± 0.0080 | 0.3239 ± 0.0154 | 0.2731 ± 0.0000 |
| Goethite | **0.0311 ± 0.0047** | 0.1006 ± 0.0000 | 0.1467 ± 0.0000 | 0.1211 ± 0.0000 | 0.2742 ± 0.0221 | 0.3150 ± 0.0106 | 0.3010 ± 0.0001 |
| Biotite | **0.0454 ± 0.0021** | 0.1219 ± 0.0000 | 0.1463 ± 0.0000 | 0.1340 ± 0.0003 | 0.2370 ± 0.0362 | 0.3649 ± 0.0123 | 0.3394 ± 0.0023 |
| Chlorite | **0.0419 ± 0.0014** | 0.0986 ± 0.0000 | 0.1466 ± 0.0000 | 0.1862 ± 0.0002 | 0.2649 ± 0.0862 | 0.3307 ± 0.0112 | 0.3563 ± 0.0004 |
| Mean | **0.0356 ± 0.0015** | 0.1073 ± 0.0000 | 0.1465 ± 0.0000 | 0.1650 ± 0.0002 | 0.2642 ± 0.0342 | 0.3336 ± 0.0098 | 0.3174 ± 0.0006 |

#### 3.1.3. Quaternary Hyperspectral Data

On the quaternary hyperspectral dataset, PIST–Net remains the best-performing blind unmixing model with mean SAD of 0.0780 and mean RMSE of 0.0802 (Tables 7 and 8). Large SAD values are concentrated within the wavelength range of 1890–2352 nm, where the absolute error in reflectance for three endmembers exceeds 0.1 (Figure 10). Although the mean RMSE of PIST–Net exceeds twice that for the ternary results, it remains within the excellent performance range of less than 0.1. To accommodate the quaternary hyperspectral data featuring 20 × 25 pixels, the patch size in this mode was set to 5 × 5. Meanwhile, a smaller patch size of 1 × 1 was also tested, though it performed slightly below the current setting. HapkeCNN and UnDIP ranked second and third in terms of performance, respectively. As shown in Figure 11, the estimated abundance map accurately reflects their true spatial features. The increase in number of endmembers indicates higher computational complexity, which can lead to a reduction in the mean RMSE representing the unmixing performance. Nevertheless, HapkeCNN and UNMamba does not strictly follow this pattern. Their mean RMSE values for quaternary data are larger than those for binary and ternary data, which may be attributed to parameter optimization under specific configurations.

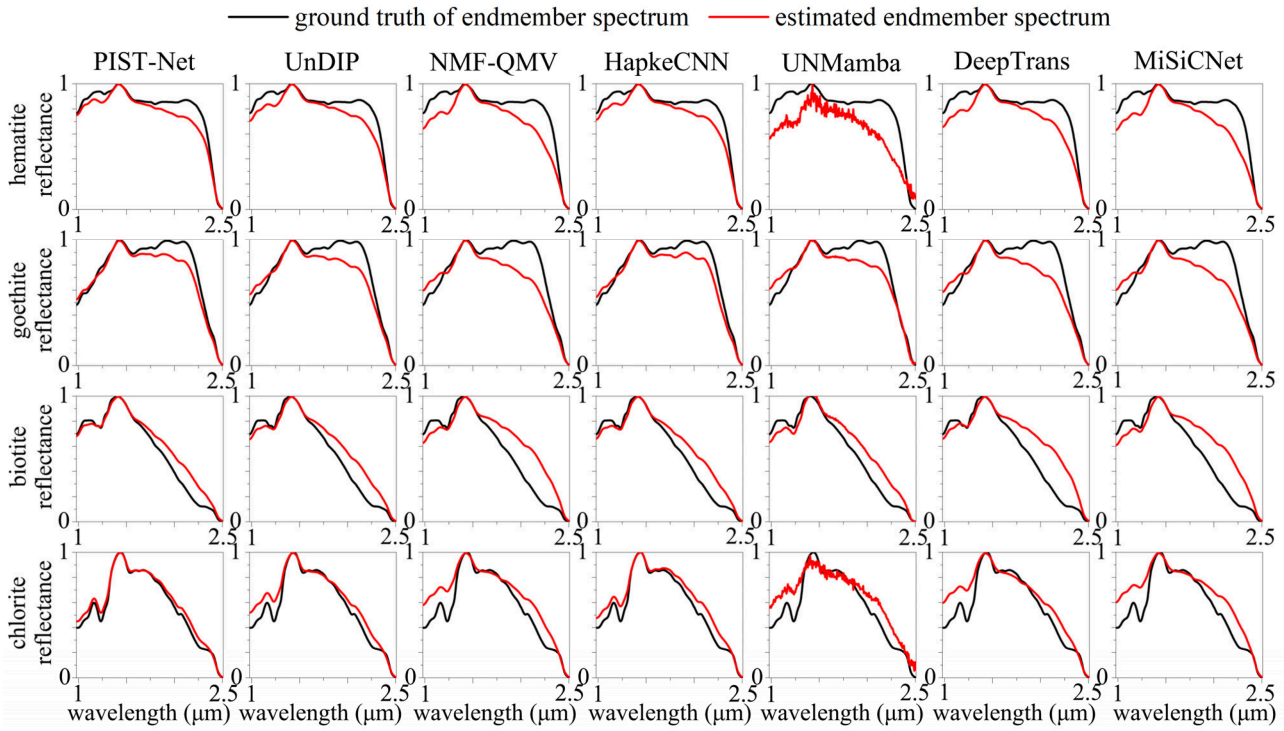


**Figure 10.** Visual comparison of estimated endmember spectra using the quaternary hyperspectral data.

**Table 7.** SAD results for the quaternary hyperspectral data (the best performances are shown in bold).

| Endmember | PIST–Net | UnDIP | NMF–QMV | HapkeCNN | UNMamba | DeepTrans | MiSiCNet |
|---|---|---|---|---|---|---|---|
| Hematite | **0.0645 ± 0.0048** | 0.0776 ± 0.0000 | 0.1285 ± 0.0000 | 0.0735 ± 0.0001 | 0.1250 ± 0.0285 | 0.1240 ± 0.0122 | 0.1374 ± 0.0000 |
| Goethite | **0.0723 ± 0.0060** | 0.1013 ± 0.0000 | 0.1522 ± 0.0000 | 0.0742 ± 0.0014 | 0.1031 ± 0.0081 | 0.1391 ± 0.0027 | 0.1612 ± 0.0000 |
| Biotite | **0.1145 ± 0.0068** | 0.1476 ± 0.0000 | 0.2229 ± 0.0000 | 0.1490 ± 0.0001 | 0.1498 ± 0.0037 | 0.1946 ± 0.0171 | 0.2351 ± 0.0000 |
| Chlorite | **0.0607 ± 0.0075** | 0.0912 ± 0.0000 | 0.1398 ± 0.0000 | 0.0789 ± 0.0001 | 0.1883 ± 0.0300 | 0.1343 ± 0.0032 | 0.1572 ± 0.0000 |
| Mean | **0.0780 ± 0.0014** | 0.1044 ± 0.0000 | 0.1608 ± 0.0000 | 0.0939 ± 0.0004 | 0.1416 ± 0.0012 | 0.1480 ± 0.0042 | 0.1727 ± 0.0000 |

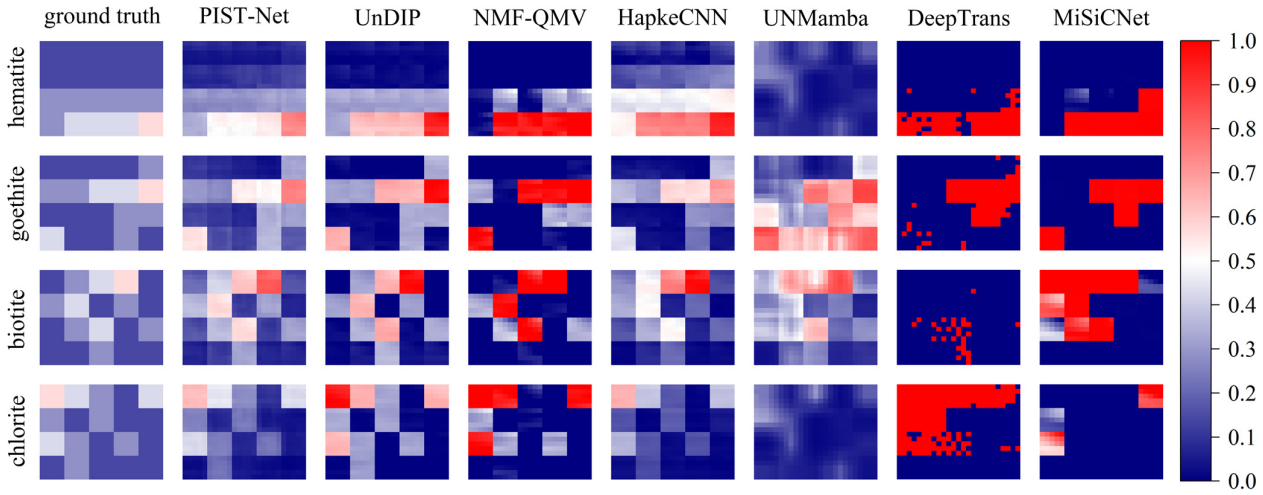


**Figure 11.** Visual comparison of estimated abundance maps using the quaternary hyperspectral data.

**Table 8.** RMSE results for the quaternary hyperspectral data (the best performances are shown in bold).

| Endmember | PIST–Net | UnDIP | NMF–QMV | HapkeCNN | UNMamba | DeepTrans | MiSiCNet |
|---|---|---|---|---|---|---|---|
| Hematite | **0.0792 ± 0.0126** | 0.1579 ± 0.0001 | 0.2718 ± 0.0000 | 0.1157 ± 0.0003 | 0.2083 ± 0.0128 | 0.4101 ± 0.0440 | 0.2701 ± 0.0000 |
| Goethite | **0.0852 ± 0.0093** | 0.1573 ± 0.0000 | 0.2730 ± 0.0000 | 0.1483 ± 0.0005 | 0.1949 ± 0.0290 | 0.3112 ± 0.0091 | 0.4170 ± 0.0000 |
| Biotite | **0.0810 ± 0.0142** | 0.1598 ± 0.0000 | 0.2740 ± 0.0000 | 0.1040 ± 0.0026 | 0.2292 ± 0.0612 | 0.3928 ± 0.0257 | 0.3366 ± 0.0000 |
| Chlorite | **0.0756 ± 0.0093** | 0.1449 ± 0.0000 | 0.2715 ± 0.0000 | 0.1968 ± 0.0024 | 0.2046 ± 0.0571 | 0.3680 ± 0.0336 | 0.3340 ± 0.0000 |
| Mean | **0.0802 ± 0.0053** | 0.1550 ± 0.0000 | 0.2726 ± 0.0000 | 0.1412 ± 0.0003 | 0.2092 ± 0.0165 | 0.3705 ± 0.0100 | 0.3394 ± 0.0000 |

### *3.2. Noisy Dataset*

Table 9 presents the results of noise tests for PIST–Net and six competing models. In addition to the clean dataset denoted as baseline, the noise tests utilized four noisy datasets with SNRs of 50 dB, 40 dB, 30 dB, and 20 dB, respectively. The results show that PIST–Net performed best on all datasets with varying levels of noise. As the SNR drops from baseline to 30 dB, the mean SAD and mean RMSE of PIST–Net increase by only 0.0016 and 0.0056, respectively. This indicates that PIST–Net shows good noise robustness with SNR below 30 dB. Compared to the results at 30 dB, the two error values under 20 dB further increase by 0.0188 and 0.0316, respectively. Such a sharp increase is primarily driven by the relative power of noise, which grows logarithmically with the SNR. As illustrated in Figure 5e, although the majority of valid information in the 20 dB data has been overwhelmed, PIST–Net still demonstrated sufficient accuracy with the mean RMSE less than 0.1.

**Table 9.** Mean SAD and RMSE results for the binary hyperspectral data with Gaussian noise (the best performances are shown in bold).

| Error | *snr* | PIST–Net | UnDIP | NMF–QMV | HapkeCNN | UNMamba | DeepTrans | MiSiCNet |
|---|---|---|---|---|---|---|---|---|
| Mean SAD | baseline | **0.0212** | 0.0323 | 0.0962 | 0.0517 | 0.0964 | 0.0757 | 0.1439 |
| | 50 dB | **0.0196** | 0.0322 | 0.0962 | 0.0517 | 0.0839 | 0.0736 | 0.1439 |
| | 40 dB | **0.0209** | 0.0327 | 0.0962 | 0.0517 | 0.1210 | 0.0745 | 0.1439 |
| | 30 dB | **0.0228** | 0.0343 | 0.0963 | 0.0528 | 0.1093 | 0.0785 | 0.1440 |
| | 20 dB | 0.0416 | **0.0378** | 0.0969 | 0.0631 | 0.1221 | 0.0751 | 0.1452 |
| Mean RMSE | baseline | **0.0312** | 0.0619 | 0.1145 | 0.1770 | 0.2467 | 0.2660 | 0.3300 |
| | 50 dB | **0.0274** | 0.0638 | 0.1145 | 0.1772 | 0.2218 | 0.2521 | 0.3300 |
| | 40 dB | **0.0311** | 0.0628 | 0.1146 | 0.1771 | 0.2998 | 0.2588 | 0.3301 |
| | 30 dB | **0.0368** | 0.0658 | 0.1149 | 0.1784 | 0.2721 | 0.2664 | 0.3297 |
| | 20 dB | **0.0684** | 0.0756 | 0.1195 | 0.1885 | 0.2953 | 0.2651 | 0.3314 |

### 3.3. RELAB Dataset

All seven models were further evaluated using the RELAB dataset acquired from the NASA Reflectance Experiment Laboratory [51]. The dataset consists of 40 spectra of mineral mixtures, with a spectral range of 320–2550 nm, 447 spectral bands, and a sampling interval of 5 nm. Four mineral endmembers are included in the dataset: olivine, plagioclase, augite, and hypersthene (Figure 12). Each spectrum of the mineral mixture was first expanded into a $5 \times 5 \times 447$ data block, and then all data blocks were arranged and combined into a $25 \times 40 \times 447$ spectral cube as the input data. In the RELAB mode, the input data of PIST–Net was linearly resampled to 256 bands to avoid additional effects. Additionally, the patch size was set to $2 \times 2$ as in binary and ternary modes.

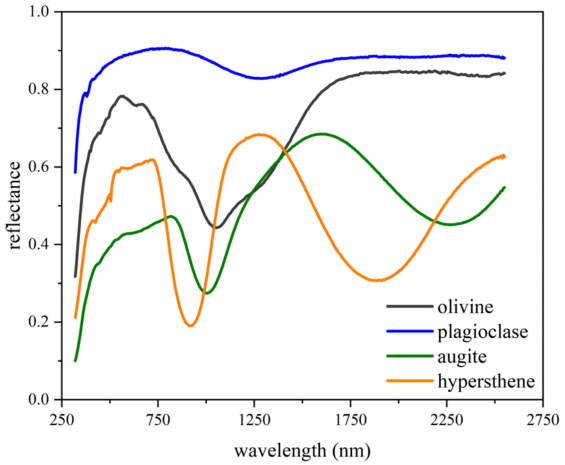


**Figure 12.** The endmember spectra in the RELAB dataset.

Figure 13 and Table 10 present the estimated abundances on the RELAB dataset. The results demonstrate that PIST–Net outperforms all competing models with a mean RMSE of 0.1091 (Figure 14). This value is larger than the 0.0802 observed in the quaternary data, which could result from the presence of pixels with varying numbers of endmembers. Among all five minerals, PIST–Net achieved the second-lowest RMSE for olivine and augite across all models, with values slightly lower than HapkeCNN and UNMamba, respectively. In the RELAB dataset, pixels with two, three, and four endmembers account for 17.5%, 62.5%, and 20% of the total pixels, respectively. The estimated abundances were further categorized and statistically analyzed by the number of endmembers, with their mean RMSEs of 0.1192, 0.1041, and 0.1030, respectively (Figure 15). These values are approximate to the mean RMSE of the entire RELAB dataset.

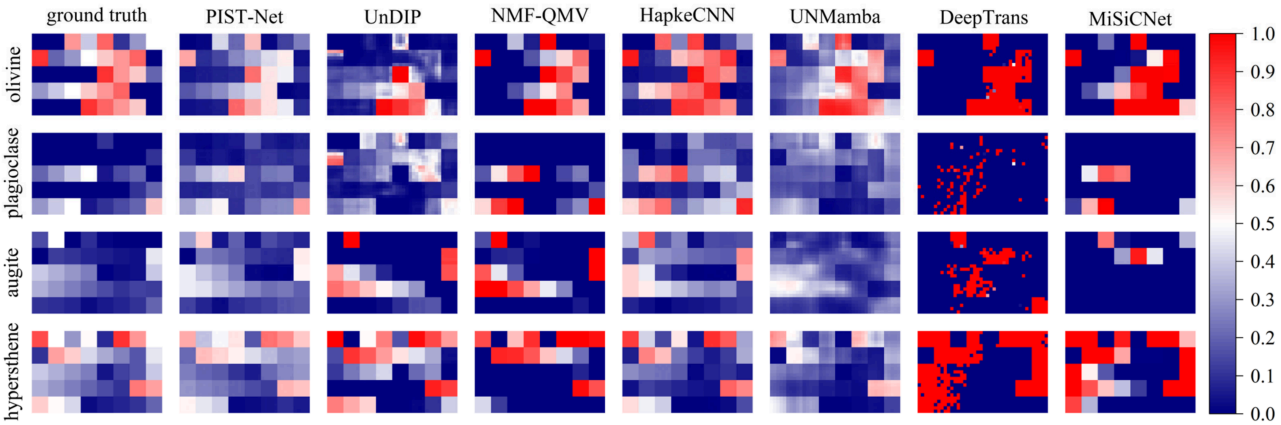


**Figure 13.** Visual comparison of estimated abundance maps using the RELAB data.

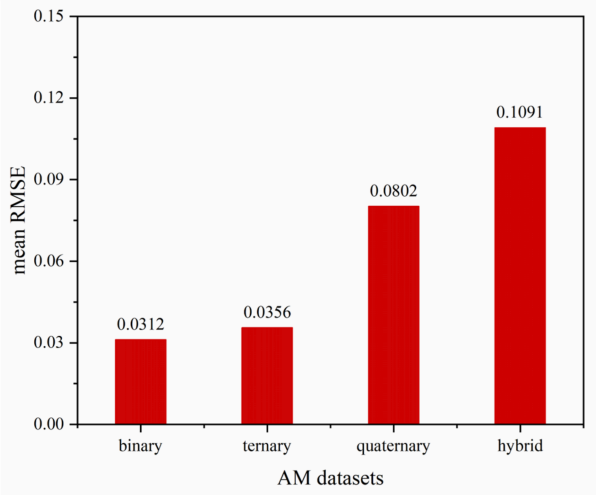


**Figure 14.** Mean RMSE of PIST–Net on different AM datasets.

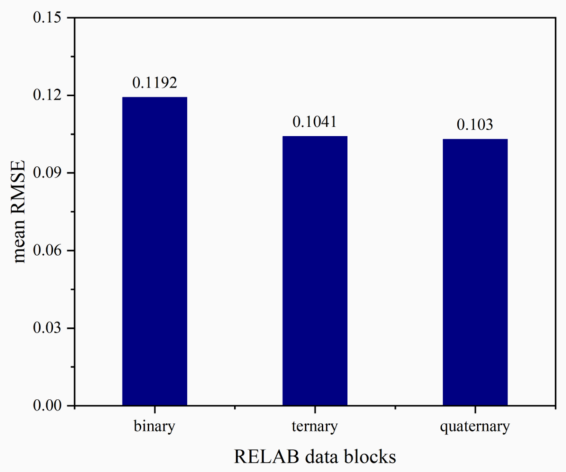


**Figure 15.** Mean RMSE of PIST–Net on different RELAB data blocks.

**Table 10.** RMSE results for the RELAB data (the best performances are shown in bold).

| Endmember | PIST–Net | UnDIP | NMF–QMV | HapkeCNN | UNMamba | DeepTrans | MiSiCNet |
|---|---|---|---|---|---|---|---|
| Olivine | 0.1533 ± 0.0083 | 0.3026 ± 0.0185 | 0.1958 ± 0.0000 | **0.0969 ± 0.0022** | 0.1750 ± 0.0020 | 0.3202 ± 0.0058 | 0.2622 ± 0.0000 |
| Plagioclase | **0.0644 ± 0.0125** | 0.2417 ± 0.0259 | 0.1841 ± 0.0000 | 0.1885 ± 0.0035 | 0.2034 ± 0.0083 | 0.3760 ± 0.0843 | 0.1501 ± 0.0000 |
| Hypersthene | **0.1120 ± 0.0118** | 0.2081 ± 0.0001 | 0.2716 ± 0.0000 | 0.1197 ± 0.0020 | 0.1293 ± 0.0139 | 0.3434 ± 0.0159 | 0.3068 ± 0.0000 |
| Augite | 0.1068 ± 0.0175 | 0.2002 ± 0.0001 | 0.2745 ± 0.0000 | 0.1546 ± 0.0033 | **0.1056 ± 0.0070** | 0.3208 ± 0.0790 | 0.2873 ± 0.0000 |
| Mean | **0.1091 ± 0.0030** | 0.2382 ± 0.0110 | 0.2315 ± 0.0000 | 0.1399 ± 0.0016 | 0.1533 ± 0.0069 | 0.3401 ± 0.0029 | 0.2516 ± 0.0000 |

## 4. Conclusions

This study presents a physics-informed Swin Transformer network, aiming to enhance the blind unmixing accuracy by incorporating the backscattering characteristics of mineral materials. A SWIR hyperspectral dataset termed AM dataset comprising hematite, goethite, biotite, and chlorite was built in a laboratory setting. The AM dataset includes binary, ternary, quaternary, and noisy data, used for the unmixing performance and noise robustness testing of PIST–Net and six existing models. All models were further evaluated on a public RELAB dataset, which equally comprises four mineral endmembers. In the results section, SAD and RMSE were used to quantify the estimation errors for endmember spectra and abundance maps, respectively.

The results show that PIST–Net consistently outperforms six competing models across all AM datasets. On the binary and ternary dataset, PIST–Net achieves excellent abundance

estimation performance. This error rises to approximately 0.1 on the quaternary and hybrid RELAB dataset, attributed to the increased unmixing complexity. Under conditions where the SNR exceeds 20 dB, PIST–Net consistently shows adequate robustness against Gaussian noise. In natural sandstone formations, the infrared spectra of altered minerals may exhibit significant differences from laboratory results, attributed to variations such as grain size, surface morphology, and complex mineral assemblages. Therefore, the performance and robustness of the blind hyperspectral unmixing algorithm still require further validation in engineering scenarios.

**Author Contributions:** Conceptualization, R.X. and H.W.; methodology, R.X.; software, R.X. and Z.Y.; validation, Z.Y., X.M. and Y.W.; formal analysis, R.X. and Z.Y.; investigation, W.W.; resources, H.W. and Y.W.; data curation, Y.W.; writing—original draft preparation, R.X.; writing—review and editing, H.W., Z.Y. and X.M.; visualization, R.X. and W.W.; supervision, Y.W.; project administration, H.W. and Y.W.; funding acquisition, H.W. All authors have read and agreed to the published version of the manuscript.

**Funding:** This research was funded by the Strategic Priority Research Program of the Chinese Academy of Sciences (grant number XDC0220100), and the National Natural Science Foundation of China (grant number 52508423).

**Data Availability Statement:** Dataset available on request from the authors.

**Conflicts of Interest:** The authors declare no conflicts of interest.

## Abbreviations

The following abbreviations are used in this manuscript:

| | |
|---|---|
| AM | Altered mineral |
| PIST–Net | Physics-informed Swin Transformer Network |
| RELAB | Reflectance Experiment Laboratory |
| RMSE | Root mean square error |
| SAD | Spectral angle distance |
| SD | Standard deviation |
| SNR | Signal-to-noise ratio |
| SSA | Single-scattering albedo |
| SWIR | Short-wave infrared |

## References

1. Radwany, M.R.; Barton, I.F. The process mineralogy of leaching sandstone-hosted uranium-vanadium ores. *Miner. Eng.* **2022**, *187*, 107811. [CrossRef]
2. Tan, Y.; Lu, L.; Yang, C.; Zhao, J.; Ding, Y. Uranium-Bearing Layers of Sandstone Type Uranium Deposits Identification and Three-Dimensional Reconstruction in the Northern Ordos Basin, North-Central China. *Minerals* **2023**, *13*, 834. [CrossRef]
3. Wang, Z.; Song, H.; Chen, Y.; Song, J.; Hou, M.; Li, Q.; Du, Q.; Yu, H. Uranium resource of Europe: Development status, metallogenic provinces and geodynamic setting. *Energy Strategy Rev.* **2024**, *54*, 101467. [CrossRef]
4. Yan, D.; Zhu, R.; Liu, W.; Liu, R.; Shou, H.; Cheng, X.; Cai, Y.; Lei, Z.; Deng, P.; Peng, Y. Metallogenic characteristics and models of sandstone-type uranium deposits in China. *Ore Geol. Rev.* **2024**, *166*, 105937. [CrossRef]
5. Coyan, J.; Solano, F.; Taylor, C.; Finn, C.; Smith, S.; Holm-Denoma, C.; Pianowski, L.; Crocker, K.; Mirkamalov, R.; Divaev, F.; et al. Tungsten Skarn Quantitative Mineral Resource Assessment and Gold, Rare Earth Elements, Graphite, and Uranium Qualitative Assessments of the Kuldjuktau and Auminzatau Ranges, in the Central Kyzylkum Region, Uzbekistan. *Minerals* **2024**, *14*, 1240. [CrossRef]
6. Zhao, J.; Liu, C. Advancements in regional geological Surveys: Insights from the 2024 China national regional geological survey conference and a six-year uranium exploration case study in Shaoguan, Guangdong. *Phys. Chem. Earth Parts A/B/C* **2025**, *139*, 103953. [CrossRef]
7. Zauner, M.; Weller, A.; Halisch, M. Laboratory core investigations of sandstone-hosted uranium for in situ recovery. *Appl. Earth Sci.* **2020**, *129*, 27–40. [CrossRef]

8. Su, X.; Liu, Z.; Yao, Y.; Du, Z. Petrology, mineralogy, and ore leaching of sandstone-hosted uranium deposits in the Ordos Basin, North China. *Ore Geol. Rev.* **2020**, *127*, 103768. [CrossRef]
9. Uren, A.L.; Laukamp, C.; George, A.D.; Occhipinti, S.A.; Aitken, A.R.A. Inferring sandstone grain size using spectral datasets: An example from the Bresnahan Group, Western Australia. *Remote Sens. Environ.* **2021**, *252*, 112109. [CrossRef]
10. Wang, Q.; Liang, X.; Wang, W.; Niu, Q.; Zhuo, J.; Su, X.; Zhou, G.; Zhao, L.; Li, P.; Yuan, W.; et al. Mineral Composition and Full-Scale Pore Structure of Qianjiadian Sandstone-Type Uranium Deposits: Application for In Situ Leaching Mining. *Geofluids* **2022**, *2022*, 2860737. [CrossRef]
11. Kurmanseiit, M.B.; Tungatarova, M.S.; Kaltayev, A.; Royer, J.-J. Reactive Transport Modeling during Uranium In Situ Leaching (ISL): The Effects of Ore Composition on Mining Recovery. *Minerals* **2022**, *12*, 1340. [CrossRef]
12. Wang, S.; Lian, M.; Ding, D.; He, G.; Fu, H. Evolution of pore structure and reactive transport parameters during acid leaching of sandstone uranium ore. *Hydrometallurgy* **2024**, *226*, 106301. [CrossRef]
13. Zhao, H.; Ao, C.; Li, J.; Chen, L.; Zhang, B.; Miao, P.; Si, Q.; Zhu, Q.; Yu, R.; Chen, Y. Occurrence and mechanism of uranium enrichment with a unique eolian sedimental environment in the Pengyang uranium deposit, Ordos Basin. *Ore Geol. Rev.* **2022**, *141*, 104641. [CrossRef]
14. Boulesteix, T.; Cathelineau, M.; Deloule, E.; Brouand, M.; Toubon, H.; Lach, P.; Fiet, N. Ilmenites and their alteration products, sinkholes for uranium and radium in roll-front deposits after the example of South Tortkuduk (Kazakhstan). *J. Geochem. Explor.* **2019**, *206*, 106343. [CrossRef]
15. Chen, L.; Chen, Y.; Guo, H.; Zhao, H.; Miao, P.; Li, J.; Feng, X.; Yu, R.; Tang, C. Characteristics of Altered Ilmenite in Uranium-Bearing Sandstone and Its Relationship with Uranium Minerals in the Northeastern Ordos Basin. *J. Earth Sci.* **2022**, *33*, 342–357. [CrossRef]
16. Ding, B.; Liu, H.; Qiu, L.; Zhang, C.; Xu, D. Ilmenite Alteration and Its Adsorption and Catalytic Reduction in U Enrichment in Sandstone-Hosted U Deposits from the Northern Ordos Basin, North China. *Minerals* **2022**, *12*, 167. [CrossRef]
17. Chen, Y.; Jin, R.; Miao, P.; Li, J.; Guo, H.; Chen, L. Occurrence of pyrites in sandstone-type uranium deposits: Relationships with uranium mineralization in the North Ordos Basin, China. *Ore Geol. Rev.* **2019**, *109*, 426–447. [CrossRef]
18. Liu, B.; Hao, P.; Zhang, Z.; Guo, X.; Zhang, P.; Shi, Z. Geology, alteration system and uranium mineralization of Tamusu large uranium deposit, China. *Ore Geol. Rev.* **2023**, *158*, 105488. [CrossRef]
19. Hu, X.; Yang, X.; Ling, M.; Xu, J.; Du, G.; Li, Q.; Cao, M.; Wu, Z. Mineralogical and geochemical studies on the Qianjiadian deposit, Songliao Basin, NE China: Insights into multiple metallogenic processes in the sandstone-type uranium deposit. *Ore Geol. Rev.* **2024**, *168*, 106050. [CrossRef]
20. Zhang, C.; Xia, F.; Deng, W.; Liu, X.; Zhang, Q.; Shi, B.; Li, H.; Fu, Y. The migration pattern of oxidation fluids and its constraints on uranium mineralization in the Tamusu sandstone type uranium deposit of the Bayingobi Basin, China. *Sediment. Geol.* **2025**, *478*, 106823. [CrossRef]
21. Chen, L.; Chen, Y.; Feng, X.; Li, J.; Guo, H.; Miao, P.; Jin, R.; Tang, C.; Zhao, H.; Wang, G.; et al. Uranium occurrence state in the Tarangaole area of the Ordos Basin, China: Implications for enrichment and mineralization. *Ore Geol. Rev.* **2019**, *115*, 103034. [CrossRef]
22. Yue, L.; Jiao, Y.; Fayek, M.; Wu, L.; Rong, H.; Xie, H. Transformation of Fe-bearing minerals from Dongsheng sandstone-type uranium deposit, Ordos Basin, north-central China: Implications for ore genesis. *Am. Mineral.* **2022**, *107*, 1396–1409. [CrossRef]
23. Lagneau, V.; Beucher, H.; Jean-Michel, S. Genetic Simulation of Roll-Front Uranium Deposits—A Reactive Transport Approach. In Proceedings of the Groundwater for a Thirsty World, Denver, CO, USA, 11–15 April 2010.
24. Pons, T.; Pagel, M.; Roy, R.; Reyx, J. Characterization of a redox front by infrared spectroscopy: A new application to a roll-front uranium deposit in Mongolia. In Proceedings of the 12th SGA Biennial Meeting, Uppsala, Sweden, 12–15 August 2013.
25. Leibold, J. Geochemistry and Mineralogy of the Alteration Halo Associated with the Three Crow Roll-Front Uranium Deposit, Nebraska, USA. Ph.D. Thesis, Colorado School of Mines, Golden, CO, USA, 2013.
26. Mathieu, R.; Deschamps, Y.; Selezneva, V.; Pouradier, A.; Brouand, M.; Deloule, E.; Boulesteix, T. Key Mineralogical Characteristics of the New South Tortkuduk Uranium Roll-Front Deposits, Kazakhstan. In Proceedings of the 13th SGA Biennal Meeting, Nancy, France, 24–27 August 2015.
27. Cuney, M.; Mercadier, J.; Bonnetti, C. Classification of Sandstone-Related Uranium Deposits. *J. Earth Sci.* **2022**, *33*, 236–256. [CrossRef]
28. Ishidoshiro, N.; Yamaguchi, Y.; Noda, S.; Asano, Y.; Kondo, T.; Kawakami, Y.; Mitsuishi, M.; Nakamura, H. Geological Mapping by Combining Spectral Unmixing and Cluster Analysis for Hyperspectral Data. *ISPRS—Int. Arch. Photogramm. Remote Sens. Spat. Inf. Sci.* **2016**, *XLI-B8*, 431–435. [CrossRef]
29. Sekandari, M.; Masoumi, I.; Pour, A.B.; Muslim, A.M.; Hossain, M.S.; Misra, A. ASTER and WorldView-3 satellite data for mapping lithology and alteration minerals associated with Pb-Zn mineralization. *Geocarto Int.* **2022**, *37*, 1782–1812. [CrossRef]
30. Soydan, H.; Koz, A.; Düzgün, H.Ş. Secondary Iron Mineral Detection via Hyperspectral Unmixing Analysis with Sentinel-2 Imagery. *Int. J. Appl. Earth Obs. Geoinf.* **2021**, *101*, 102343. [CrossRef]

31. Rajendran, S.; Nasir, S. Mapping of hydrothermal alteration in the upper mantle-lower crust transition zone of the Tayin Massif, Sultanate of Oman using remote sensing technique. *J. Afr. Earth Sci.* **2019**, *150*, 722–743. [CrossRef]
32. Abubakar, A.; Hashim, M.; Pour, A.B. Identification of hydrothermal alteration minerals associated with geothermal system using ASTER and Hyperion satellite data: A case study from Yankari Park, NE Nigeria. *Geocarto Int.* **2019**, *34*, 597–625. [CrossRef]
33. Esmaeilzadeh, N.; Barak, S.; Gani, N.D.; Imamalipour, A.; Abedi, M.; Pour, A.B. Alteration Zones Detection Using Image-Based and Spectrum-Based Image Processing Techniques to Aster Data: Sonajil Copper Deposit. In Proceedings of the IGARSS 2023—IEEE International Geoscience and Remote Sensing Symposium, Pasadena, CA, USA, 16–21 July 2023.
34. Arjmand Lary, Z.; Honarmand, M.; Shahriari, H.; Hosseinjani Zadeh, M. Data Integration by Fuzzy Logic for Mineral Prospectivity Mapping in Ferdows–Gonabad–Bajestan Belt, Khorasan Razavi Province, Iran. *J. Indian Soc. Remote Sens.* **2024**, *52*, 1223–1243. [CrossRef]
35. Esmaeili, M.; Fathianpour, N.; Soltani-Mohammadi, S. PRISMA hyperspectral imagery for mapping alteration zones associated with Kuhpanj porphyry copper deposit, Southern Iran. *Eur. J. Remote Sens.* **2024**, *57*, 2299369. [CrossRef]
36. Karimzadeh, S.; Tangestani, M.H.; Fonseca, A. The synergistic use of WorldView-3 and EO1-Hyperion data for the identification of lineaments and hydrothermal alteration minerals in the Chadormalu iron oxide-apatite deposit area, Central Iran. *Earth Sci. Inform.* **2023**, *16*, 2573–2593. [CrossRef]
37. Muavhi, N. Application of per-pixel and sub-pixel unmixing methods on ASTER images to map hydrothermal alterations in a highly metamorphosed terrain: A case of the Musina copper deposit field. *Geocarto Int.* **2022**, *37*, 13579–13595. [CrossRef]
38. Moghadam, H.J.; Oskouei, M.M.; Nouri, T. Unmixing of hyperspectral data for mineral detection using a hybrid method, Sar Chah-e Shur, Iran. *Arab. J. Geosci.* **2020**, *13*, 1041. [CrossRef]
39. Barker, R.D.; Barker, S.L.L.; Cracknell, M.J.; Stock, E.D.; Holmes, G. Quantitative Mineral Mapping of Drill Core Surfaces II: Long-Wave Infrared Mineral Characterization Using μXRF and Machine Learning. *Econ. Geol.* **2021**, *116*, 821–836. [CrossRef]
40. Yousefi, M.; Tabatabaei, S.H.; Rikhtehgaran, R.; Pour, A.B.; Pradhan, B. Application of Dirichlet Process and Support Vector Machine Techniques for Mapping Alteration Zones Associated with Porphyry Copper Deposit Using ASTER Remote Sensing Imagery. *Minerals* **2021**, *11*, 1235. [CrossRef]
41. Fereydooni, H.; Moradzadeh, A.; Pahlavani, P.; Mojeddifar, S. Full unmixing hydrothermal alteration minerals mapping by integration of pattern recognition network and directed matched filtering algorithm. *Earth Sci. Inform.* **2020**, *13*, 417–431. [CrossRef]
42. Kai, Q.; Yingjun, Z.; Ling, Z.; Yuechao, Y.; Xin, C. Depth feature extraction for mineral mixed spectrum analysis based hyperspectral data. In Proceedings of the Seventh Symposium on Novel Photoelectronic Detection Technology and Applications, Kunming, China, 5–7 November 2020.
43. Hapke, B. Bidirectional reflectance spectroscopy: 1. *Theory. J. Geophys. Res. Solid Earth* **1981**, *86*, 3039–3054. [CrossRef]
44. Rasti, B.; Koirala, B.; Scheunders, P.; Ghamisi, P. UnDIP: Hyperspectral Unmixing Using Deep Image Prior. *IEEE Trans. Geosci. Remote Sens.* **2022**, *60*, 5504615. [CrossRef]
45. Heylen, R.; Burazerovic, D.; Scheunders, P. Fully Constrained Least Squares Spectral Unmixing by Simplex Projection. *IEEE Trans. Geosci. Remote Sens.* **2011**, *49*, 4112–4122. [CrossRef]
46. Zhuang, L.; Lin, C.; Figueiredo, M.A.T.; Bioucas-Dias, J.M. Regularization Parameter Selection in Minimum Volume Hyperspectral Unmixing. *IEEE Trans. Geosci. Remote Sens.* **2019**, *57*, 9858–9877. [CrossRef]
47. Rasti, B.; Koirala, B.; Scheunders, P. HapkeCNN: Blind Nonlinear Unmixing for Intimate Mixtures Using Hapke Model and Convolutional Neural Network. *IEEE Trans. Geosci. Remote Sens.* **2022**, *60*, 5536315. [CrossRef]
48. Chen, D.; Zhang, J.; Li, J. UNMamba: Cascaded Spatial–Spectral Mamba for Blind Hyperspectral Unmixing. *IEEE Geosci. Remote Sens. Lett.* **2025**, *22*, 5502405. [CrossRef]
49. Ghosh, P.; Roy, S.K.; Koirala, B.; Rasti, B.; Scheunders, P. Hyperspectral Unmixing Using Transformer Network. *IEEE Trans. Geosci. Remote Sens.* **2022**, *60*, 5535116. [CrossRef]
50. Rasti, B.; Koirala, B.; Scheunders, P.; Chanussot, J. MiSiCNet: Minimum Simplex Convolutional Network for Deep Hyperspectral Unmixing. *IEEE Trans. Geosci. Remote Sens.* **2022**, *60*, 5522815. [CrossRef]
51. Milliken, R. Spectral Library Bundle of Reflectance Spectra and Ancillary Data Acquired by RELAB at Brown University. 2020. Available online: https://pds-speclib.rsl.wustl.edu/search.aspx?catalog=RELAB (accessed on 5 May 2026).


**Disclaimer/Publisher's Note:** The statements, opinions and data contained in all publications are solely those of the individual author(s) and contributor(s) and not of MDPI and/or the editor(s). MDPI and/or the editor(s) disclaim responsibility for any injury to people or property resulting from any ideas, methods, instructions or products referred to in the content.